Time Scales of Clouds and Cloud-Controlling Variables in Subtropical Stratocumulus from a Lagrangian Perspective

RYAN EASTMAN, ROBERT WOOD, AND CHRISTOPHER S. BRETHERTON

Department of Atmospheric Sciences, University of Washington, Seattle, Washington

(Manuscript received 9 February 2015, in final form 15 April 2016)

ABSTRACT

The Lagrangian evolution of cloud cover and cloud-controlling variables is well approximated using red noise processes with different autocorrelation time scales for each variable. Trajectories within the subtropical marine boundary layer are generated using winds from ECMWF Re-Analysis data for low cloud decks in four eastern subtropical ocean basins. Cloud cover, liquid water path, and boundary layer depth are sampled at 12-h intervals using A-Train satellites, and droplet concentration is sampled every 24 h. Lower-tropospheric stability and vertical velocity are sampled concurrently using reanalysis data. Samples are converted to seasonal and diurnal anomalies. Data are spatially averaged over a range of length scales. The e-folding decay times τ for autocorrelation are calculated for each variable based on lag times of 12, 24, 36, and 48 h. Using lag 24 h and an averaging radius of 100 km, $\tau \approx 15$–17 h for liquid water path and vertical velocity, $\tau \approx 19$ h for cloud cover, $\tau \approx 24$–25 h for boundary layer depth and droplet concentration, and $\tau \approx 53$ h for lower-tropospheric stability.

Time scales vary somewhat between regions and are shortest in the eastern Indian Ocean. Decay time τ increases with averaging scale and the autocorrelation e-folding length of a variable at a fixed time. Diurnal analysis shows cloud cover anomalies have a stronger memory during morning breakup, while other variables show stronger memory as clouds reform in the evening. Lagrangian cloud anomalies are less persistent than anomalies at a fixed location. For the latter, estimated τ values can vary significantly at different lag times, so a red noise assumption is inappropriate.

1. Introduction

Eastman and Wood (2016, hereinafter EW16) studied cloud responses in subtropical marine stratocumulus (Sc) regimes to controlling variables using the Lagrangian perspective, following the flow within the planetary boundary layer (PBL). To compare changes between sets of trajectories over time, they found that it was necessary to account for memory effects in cloud-related quantities, such as cloud cover, droplet concentration (N_d), and liquid water path (LWP). They used a linear regression approach to estimate and correct for these effects. In this work, we show that these memory effects are well described as red noise processes, in which anomalies are damped on quantifiable characteristic time scales. Anomalies for each variable are defined as the departure from the seasonal and diurnal mean for the location sampled.

Red noise processes with robust decorrelation time scales (Hasselmann 1976; Jenkins and Watts 1968; Mann and Lees 1996; von Storch and Zwiers 1999; Wunsch 1999) have been observed in the atmosphere with time scales ranging from seconds for small-scale turbulence (Hanna 1981) to hours or days for midlatitude boundary layer cloud cover (Mauger and Norris 2010) to decades or centuries for large-scale climate variability (Roe 2009). Roe (2009) posits that red noise processes should be considered the null hypothesis for geophysical time series in general. Hanna (1981) and Mauger and Norris (2010) both compared Lagrangian decorrelation time scales (following the flow) to Eulerian time scales (at a fixed location) and found that Lagrangian time scales were longer.

The over 62 000 individual trajectories studied by EW16 create an unparalleled resource for studying Lagrangian evolution of subtropical marine boundary layer clouds and their controlling variables. We estimate decorrelation time scales for different cloud and cloud-controlling variables

Corresponding author address: Ryan Eastman, Dept. of Atmospheric Sciences, University of Washington, Box 351640, Seattle, WA 98195.
E-mail: rmeast@atmos.washington.edu

DOI: 10.1175/JAS-D-16-0050.1

associated with Sc clouds and their controls as a function of averaging length scale for downstream evolution times up to 48 h. We interpret these Lagrangian time scales and compare them with corresponding Eulerian time scales, reaching different conclusions than Mauger and Norris (2010).

2. Data

All data for this study are for the years 2007–08. Data fields are for twice-daily retrievals, one for day (1330 local time) and one for night (0130 local time) on a 1° × 1° grid. The grid is chosen to match the Moderate Resolution Imaging Spectroradiometer (MODIS) level-3 (L3) 1° × 1° grid with grid box centers at the half-degree (e.g., latitude 20.5°N, longitude 145.5°W). Reanalysis data grids are originally for observation times of 0000, 0600, 1200, and 1800 UTC, so observation times are interpolated to match the timing of the A-Train observations where necessary. Zenith angle biases seen in the MODIS data products have been removed using the same technique as in EW16.

a. Data unchanged from EW16

The majority of the data used in this study are identical to those used in EW16, to which the reader is referred for more detail about the processing of these products. Cloud cover data come from the MODIS L3 cloud mask product (MYD08-D3; Hubanks et al. 2008; Oreopoulos 2005). Liquid water path retrievals come from the Advanced Microwave Scanning Radiometer for Earth Observing System (AMSR-E; Wentz and Meissner 2004) for day and night. Lower-tropospheric stability (LTS), our chosen proxy for inversion strength, is defined as the difference between potential temperature at 700 hPa and at 2 m ($\theta_{700} - \theta_{2m}$). At the trajectory beginning (0 h), LTS is derived from the ECMWF-Auxiliary dataset (Partain 2007), which provides ECMWF Re-Analysis data specifically along the *CloudSat*/*Cloud–Aerosol Lidar and Infrared Pathfinder Satellite Observations* (*CALIPSO*) track. Farther along in the trajectories, at observation hours greater than 0, θ_{700}, and θ_{2m} are obtained from the ERA-Interim data fields (Dee et al. 2011).

Droplet concentration N_d is derived from two MODIS level-3 products: cloud droplet effective radius r_e and liquid water path for cloudy pixels only. Both LWP and r_e are from the MODIS cloud optical properties product (King et al. 2003; Platnick et al. 2003). We use the same relationship as shown in Eq. (1) of EW16 to derive N_d.

We use the same regions of study as shown in Fig. 1 of EW16 (also Fig. 4 in this paper), located in the eastern subtropics of the North and South Pacific, the South Atlantic, and the Indian Ocean and the same ~62 000 trajectories, computed as in EW16 and Bretherton et al. (2010) using the 925-hPa wind from ERA-Interim. We only study trajectories advecting toward the west in order to minimize the number of samples that are influenced by meteorology associated with the westerly storm tracks.

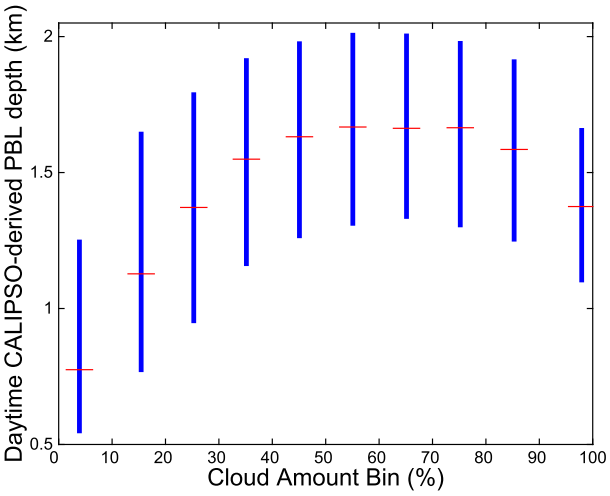

FIG. 1. Median (red dashes) and interquartile range (blue boxes) for daytime boundary layer depths for bins of percent cloud cover. Boundary layer depth derived from the *CALIPSO* vertical feature mask product, cloud amount from MODIS cloud mask.

b. Vertical velocity ω at 850 mb

Myers and Norris (2013) show that vertical velocity on the mesoscale (scales of ~100 km) is a significant cloud-controlling variable. For this work, vertical pressure velocity ω (Pa s^{-1}) at 850 mb is taken from the ERA-Interim (Dee at al. 2011) on a 1° × 1° grid.

c. Planetary boundary layer depth

As described in EW16, we use the Cloud–Aerosol Lidar with Orthogonal Polarization (CALIOP) carried on the *CALIPSO* to produce an initial estimate of PBL depth at the beginning of each trajectory using the vertical feature mask product (Vaughan et al. 2004).

For this study, we also wish to analyze how PBL depth changes along trajectories, as PBL depth has been shown to be an important cloud-controlling variable (Bretherton and Wyant 1997; Berner et al. 2013). Specifically, we are interested in how fast PBL height anomalies along trajectories decorrelate with time. Because the *CALIPSO* data are too sparse for this purpose, we also estimate PBL depth based on cloud-top temperature retrieved from MODIS, which samples a much broader swath width under the A-Train orbits. We use the *CALIPSO* retrievals of cloud-top height to test and calibrate the MODIS retrievals, as detailed in the remainder of this section.

Figure 1 shows the median and interquartile range for our *CALIPSO*-derived PBL depth (CPBL) for bins of

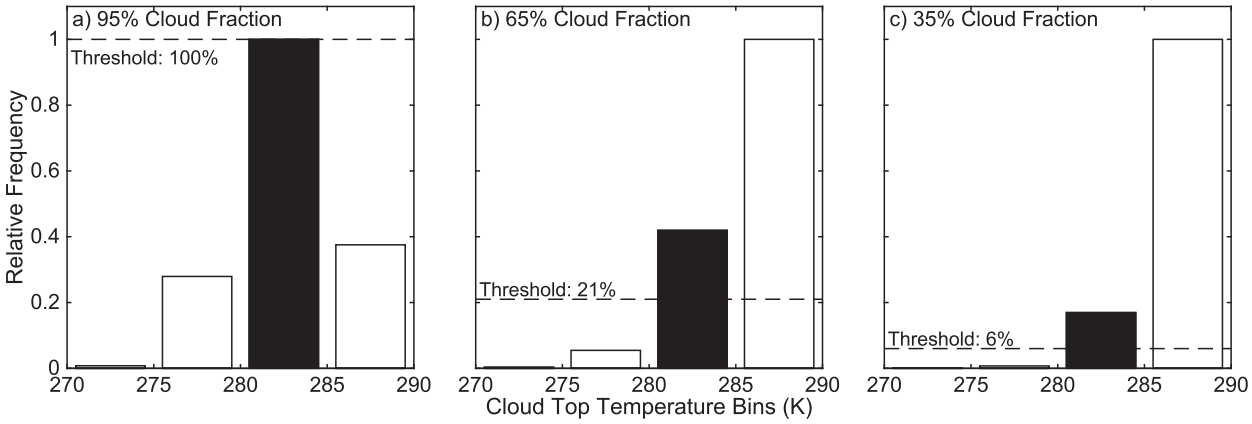

FIG. 2. Composite frequency distributions of cloud-top temperature bins for pixels within 1° × 1° grid boxes for our regions of study. Distributions are shown for bins of nighttime cloud cover: (a) 90%–100%, (b) 60%–70%, and (c) 30%–40%. Sampling thresholds for each bin of cloud cover are shown as the dashed line. The black bar on the histogram represents the assigned cloud-top temperature for clouds at the PBL top for each cloud cover bin. Mean distributions are for all available grid boxes in our study regions during the first five days of 2007.

percent cloud cover from MODIS (CC) during the day. The figure shows overcast conditions associated with shallow boundary layers, with the CPBL increasing as CC declines from 100% until around 50%, when CPBL decreases as CC declines further. This is consistent with the physical model proposed for the evolution of cloud cover and PBL depth by Wyant et al. (1997): Sc decks originate as shallow, unbroken cloud decks, but the Sc begins to break up after the PBL deepens and decouples, leaving behind shallow trade cumulus (Cu). This relationship is also shown nicely by Karlsson et al. (2010).

To track the evolution of PBL depth, we expand the sampling from the *CALIPSO* curtain using fields of cloud-top temperature (CTT) and sea surface temperature (SST). Sea surface temperature data come from the ERA-Interim 1° × 1° grids and CTT profiles (histograms) on the 1° × 1° grid come from MODIS (King et al. 2003). CTT profiles are only used if there are no samples within a box with temperatures below 0°C. For each sample, we calculate the temperature difference ΔT between the surface and cloud top. We then use the lapse rate parameterization presented in Wood and Bretherton (2004, their Fig. 4) to estimate the lapse rate for each sample (Γ; K km^{-1}). Cloud-top height H is then calculated as $H = \Delta T/\Gamma$.

CALIPSO and MODIS cloud-top height (CTH) inferred PBL depths (shortened to just "PBL depth" or "CTH PBL depth") are most directly comparable for overcast conditions, where the cloud top is generally smoother, there are no cloud edges, and fewer thin spots where the MODIS CTT retrievals could be biased by a warmer surface below. In overcast conditions, we assume that the largest peak in CTT histograms represents the temperature at the top of the PBL. Overcast MODIS-derived PBL (MPBL) depths tended to be 100–200 m deeper than their collocated *CALIPSO* equivalents. The difference in overcast CPBL and MPBL values may be due to the relative coarseness of the CTT histograms, which are for 5-K bins, meaning a possible (though highly unlikely) error of nearly 1 km, although actual discrepancies between MPBL and CPBL estimates were not nearly that large. Differences could also be the result of small calibration errors. For our finished MPBL product, we apply a correction to the MPBL data, subtracting the mean difference between overcast MPBL and CPBL from the MPBL data for all cloud amounts. This "calibration correction" is uniform in space and time and for all cloud amounts.

In more broken cloud scenes, we assume that the top of the PBL is colder than the most populous CTT bin in each histogram, owing to the increased prevalence of thin clouds and cloud edges in the sample. For retrievals with less than overcast cloud cover we "tune" the histogram sampling by decreasing the sampling threshold on the cold side of the peak as cloud fraction declines in order to match the curve between the *CALIPSO* CTH inferred PBL and cloud amount shown in Fig. 1. Further below, we describe the iterative process used to determine the sampling threshold. Our sampling method is illustrated in Fig. 2. Three composite histograms representing the mean distribution for all available 1° × 1° boxes within our regions over five days are shown. Each bar represents the relative frequency of occurrence for subgrid pixels within the L3 1° × 1° grid that have a CTT in the specified 5-K bin. Figure 2a shows a CTT histogram for overcast conditions (CC > 90%). The black bar represents the peak in the sample, which we assign as the CTT for the sample. Figure 2b shows a CTT histogram

TABLE 1. Sampling thresholds for cloud-top temperature histograms used to derive PBL depths from MODIS. Percentages represent the minimum height (relative to the highest peak in the distribution, on the cold side of the peak) that a histogram bin must achieve to represent the cloud-top temperature at the inversion top. See Fig. 2.

Day		Night	
Cloud amount	Sampling threshold	Cloud amount	Sampling threshold
		30%–40%	6%
30%–50%	7%	40%–50%	8.5%
50%–60%	9%	50%–60%	14%
60%–70%	14%	60%–70%	21%
70%–80%	19.5%	70%–80%	27%
80%–90%	32%	80%–90%	45%
90%–100%	100%	90%–100%	100%

for 60%–70% cloudy conditions, where we assume that the top of the PBL is only observed in some of the pixels within the 1° grid box of the L3 data, while more pixels represent broken or thin clouds with an emissivity <1. We have determined (using the process described below) that the representative CTT for the PBL top in 60%–70% cloudy conditions is the histogram bar farthest on the cold side of the peak that is at least 21% as high as the peak. Figure 2c shows a histogram for 30%–40% cloudy conditions where we adjust the sampling even more toward the cold side of the plot, choosing the leftmost bar that is at least 6% as high as the peak.

The thresholds for this sampling method were determined using an iterative process where, for each 10% bin (from 30%–90%) of cloud cover, we altered the sampling threshold until the CC versus MPBL curve matched the curve shown in Fig. 1 of CC versus CPBL. This was done for day and night separately. Sampling thresholds are shown in Table 1. This iterative process guarantees that the CC versus PBL depth relationship is unbiased for our MPBL product. Figure 3 shows the MODIS- and *CALIPSO*-derived PBL depths for day (Fig. 3a) and night (Fig. 3b) separately before the calibration correction and combined (Fig. 3c) after the calibration correction, verifying that the CC versus PBL depth relationship is consistent between both datasets. Figure 3d shows the correlation coefficient between vectors of collocated MPBL and CPBL samples for day and night for bins of sample cloud cover. All correlations are above $r = 0.45$.

We do not estimate an MPBL for samples with cloud amounts below 30%, since correlation coefficients drop below 0.4 and the sampling thresholds appear unreasonably small. A slight zenith angle correction has also been applied to the MPBL data, which showed a high bias at wide viewing angles. MPBL data with viewing angles above 60° have been excluded, since the zenith angle bias at those angles appeared disproportionally large (excluding only the farthest 7°). Contour maps for climatologies of the MPBL product are shown for each region in Fig. 4. Figure 4 compares favorably to other studies showing PBL depth and cloud-top heights, specifically Fig. 5 of Sun-Mack et al. (2014), which shows a

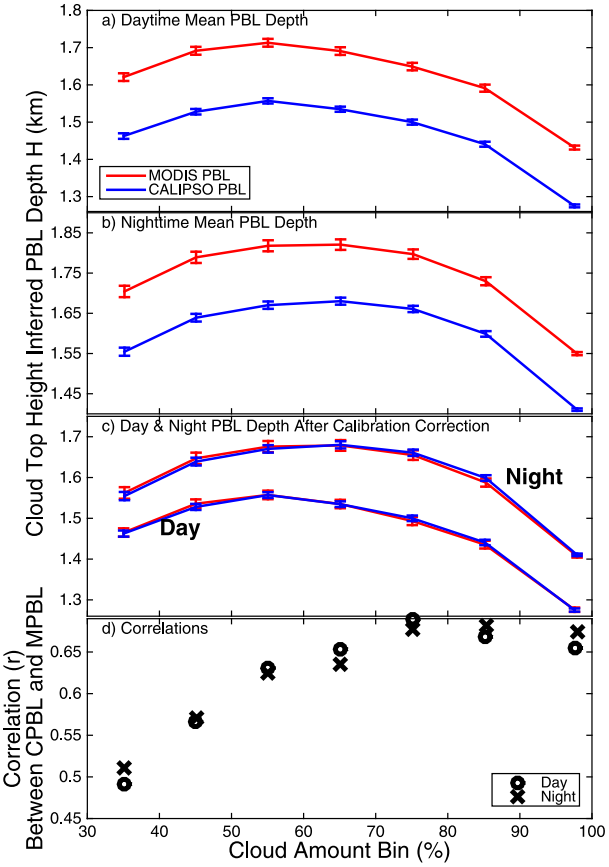

FIG. 3. (a) Day and (b) night comparison of PBL depths from all available *CALIPSO* and MODIS observations with 2-sigma standard-error bars for 10% bins of cloud cover. (c) Day and (d) night correlation between vectors of collocated CPBL and MPBL depths for 10% bins of cloud cover.

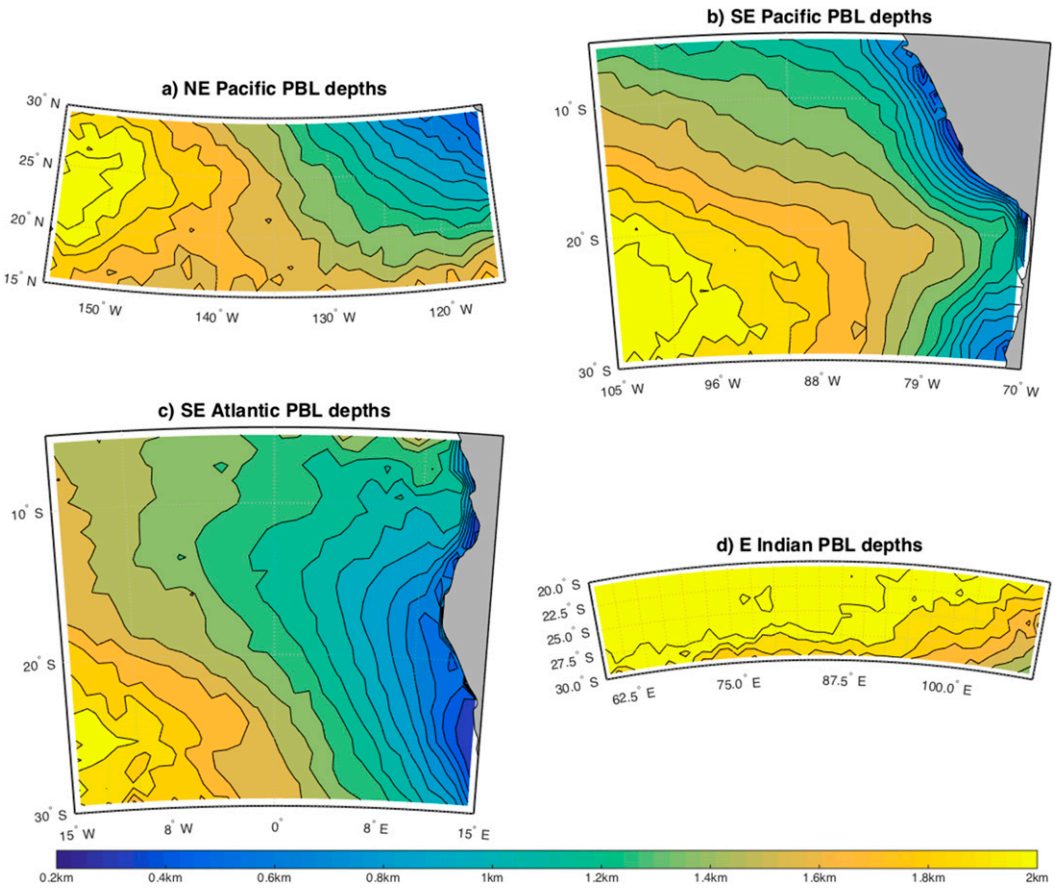

FIG. 4. Climatological average, cloud-top height inferred, MODIS-derived PBL depths for our four regions of study for all available data during the years 2007–08.

global, seasonal breakdown of single-layer cloud-top heights based on a geographically varying lapse rate, and Chan and Wood (2013, their Fig. 5), who used COSMIC GPS radio occultation to identify moisture hydrolapses that typically mark the top of the PBL. In subtropical eastern ocean basins, all three studies show shallower boundary layers near the coast with ''tongues'' of shallow PBLs extending offshore with the mean flow. All three studies also show cloud-top height/PBL depths ranging from about 0.5 km near the coast to around 2 km offshore, with deeper PBLs in the eastern Indian Ocean relative to our other study areas.

3. Methods

a. Calculating anomalies

The distributions of cloud cover and cloud-controlling variables are not uniform across our study regions, nor are the lengths of our trajectories. As a consequence of this nonuniformity, we cannot directly compare cloud changes between trajectories. Some trajectories may show large changes if they advect across a region that shows a strong climatological change, while others may show little to no change if they travel only a short distance or span a region with more uniform cloud properties. To account for this, we follow EW16 and convert all variables that are tracked along the trajectories to anomalies, which are calculated by removing the seasonal mean for day and night separately.

b. Maximizing available data

Trajectories are all run from 0 h (T0) to 48 h (T48). To maximize the data available, for each variable we examine every possible 12-, 24-, or 36-h change. The 12-h changes comprise changes from T0 to T12, T12 to T24, T24 to T36, and T36 to T48. The 24-h changes are made up of T0 to T24, T12 to T36, T24 to T48, etc.) Because of this, we have 4 times as many 12-h changes as trajectories.

c. Calculating e-folding times using a red noise assumption

A red noise (AR1) process generates a statistically stationary time series having a zero mean, constant

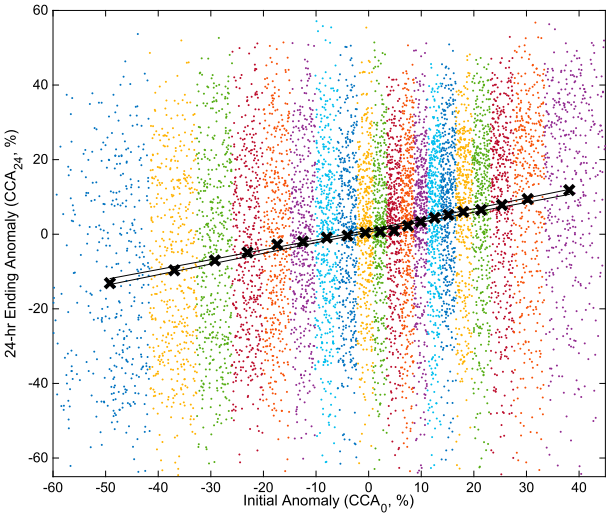

FIG. 5. Cloud cover anomalies sampled at 0 h vs those sampled again at 24 h along every 15th trajectory. Bins of starting cloud anomalies are shown by different colors. Bin means for CCA_0 and CCA_{24} are shown as crosses. The confidence interval showing the 2-sigma bounds of a linear fit to the means is plotted with a black line.

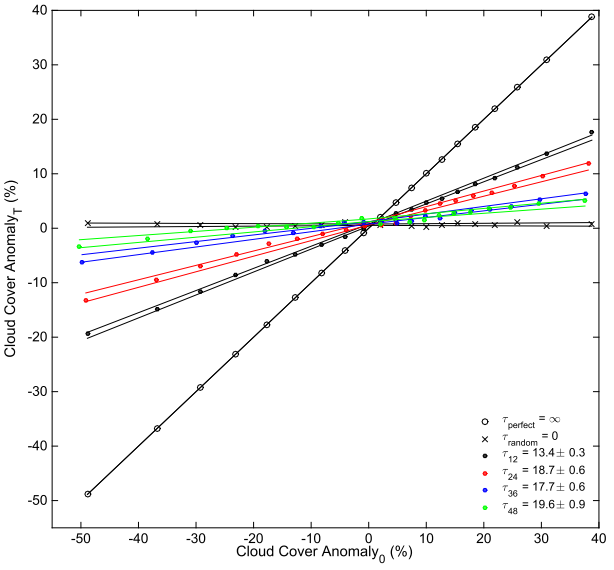

FIG. 6. Bin-mean cloud cover anomalies at 0 h vs bin-mean cloud cover anomalies at T hours for all available trajectories. The e-folding times (τ_T) for specific lag times T are shown in the legend. Also shown are a 1:1 line showing a plot of 0-h observations matched with themselves (τ_{perfect}) and a flat line showing a plot of 0-h observations randomly matched with 12-h end points (τ_{random}). The 2-sigma confidence intervals are shown for each lag time and incorporated into the errors shown in the τ values in the legend.

variance, and samples that are correlated in time through partial persistence of the signal, unlike white noise, which is uncorrelated in time. Red noise time series show an exponential decrease of autocorrelation at longer lag times (Von Storch and Zwiers 1999). Given samples with a particular lag T at which the lagged autocorrelation is found to be $r(T)$, the e-folding time τ that it takes for the lag correlation to decline by a factor of $1/e$ can be calculated:

$$\tau = \frac{-T}{\log[r(T)]}. \tag{1}$$

For a red noise process, the estimated τ should be independent of the lag T used to estimate it.

Figure 5 shows an example of how we estimate $r(T)$ from our data, which encompasses anomaly time series for thousands of trajectories, for the case of cloud cover and a lag $T = 24$ h. It shows a scatterplot of initial cloud cover anomalies (CCA_0) along the x axis and their corresponding 24-h anomalies (CCA_{24}) upon resampling of the trajectories. We sample a circular region with a radius of 100 km around each sample point along our trajectories. To reduce clutter, we only plot every 15th point. We split the trajectories into 20 bins of CCA_0 with an equal number of trajectories in each bin. Bins are shown by the differences in color in the scatterplot. The means of CCA_0 and CCA_{24} are marked with an "x" within each bin. An estimate of the slope and a representation of the error (discussed below) is shown by the black lines.

If CCA_t is approximately a red noise time series, we expect that this scatterplot will have a linear fit whose slope is the correlation coefficient $r(T)$ (von Storch and Zwiers 1999, p. 150). The binning by CCA_0 shows that such a linear relationship does exist. Using standard formulas from linear regression, we also calculate sampling error in the estimated slope $r(T)$. Figure 5 shows the two-standard-deviation confidence range of the slope.

4. Results

In Fig. 6, we apply the same technique shown in Fig. 5 to CCA for all lags ($T = 12$, 24, 36, and 48 h) sampled by our trajectories. The sampling radius is also 100 km. The scatterplots are omitted, but the bin means are still shown as well as the confidence interval. Figure 6 shows that, for all sampling lags, there is a linear relationship between CCA_0 and CCA_T, with the slope decreasing for longer lag times. Also shown are two reference lines, one showing initial anomalies matched with themselves, which represents a system with perfect memory [$r(T) = 1$], and another showing our analysis carried out for randomly matched start and end points [$r(T) = 0$].

The e-folding times τ in hours estimated from these lags are noted in the legend of Fig. 6. Their confidence intervals are deduced from those of $r(T)$. The estimates

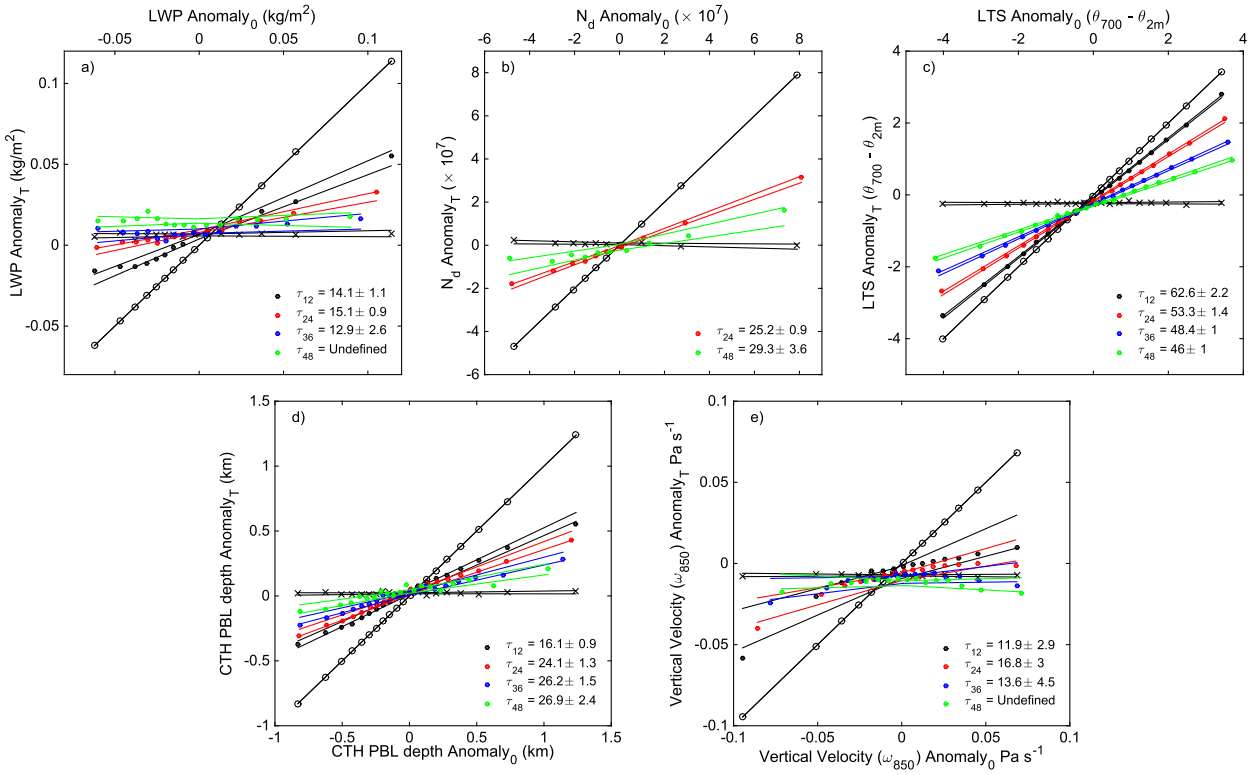

FIG. 7. As in Fig. 6, but for anomalies of (a) liquid water path, (b) droplet concentration N_d, (c) lower-tropospheric stability, (d) cloud-top height inferred boundary layer depth, and (e) 850-mb vertical velocity ω.

of τ using lags of 24 h or longer are not statistically distinguishable, consistent with a red noise process. However, the estimated τ is somewhat lower for a lag of 12 h. Since cloud cover has a substantial diurnal cycle, its anomalies are perhaps poorly modeled as a red noise process on subdiurnal time scales.

Figure 7 uses the same conventions as Fig. 6, but for anomalies of LWP (Fig. 7a), N_d (Fig. 7b), LTS (Fig. 7c), cloud-top height inferred PBL depth (Fig. 7d), and ω (Fig. 7e). There are fewer bins for the N_d plot as a result of the daytime-only data availability, which halves our number of available trajectories. Except for ω, the plots show overwhelmingly linear relationships between initial and ending mean anomalies for each variable. Vertical motion is unique in showing curved lines in these plots, which we interpret as negative ω anomalies (upward motion) being more persistent than positive ω anomalies (downward motion). This is reflected in larger error bounds on the red noise fits τ for ω throughout.

The thick shaded lines on Fig. 8 show the range of τ values for all of our tracked variables at each lag time based on the confidence intervals estimated in Figs. 6 and 7. Significant differences in τ values are seen between most variables. Liquid water path and ω have the shortest estimated *e*-folding times ($\tau \approx$ 12–17 h), meaning LWP and ω anomalies change quickly relative to other variables following the flow. Cloud cover shows a marginally longer τ of 14–20 h. Droplet concentration and PBL depth show yet longer τ values of 24–29 h, except for PBL depth at 12 h, which curiously shows a much lower τ of only 16 h, similar to the shorter τ seen for cloud cover at 12 h. Tropospheric stability shows by far the longest *e*-folding time, with τ between two and three days.

Confidence intervals for ω and LWP expand noticeably with longer lag times, even overlapping with zero at 48 h. This is because of the lagged autocorrelations degrading to nearly zero after 48 h, since τ values are only around 14–20 h. Except for LTS, most of the plots are nearly flat from 24 to 48 h. The relative invariance of τ for changing lag times shows that the red noise assumption is reasonable for these variables in the Lagrangian perspective. Lower-tropospheric stability is unique in showing a decline in τ with increasing lag times, suggesting that the temporal behavior of LTS along trajectories is less well represented by a red noise assumption.

a. Diurnal dependence

Figure 9 uses the same conventions as Fig. 8 but shows *e*-folding times for each variable separated by whether trajectories began during the day or night. The darker

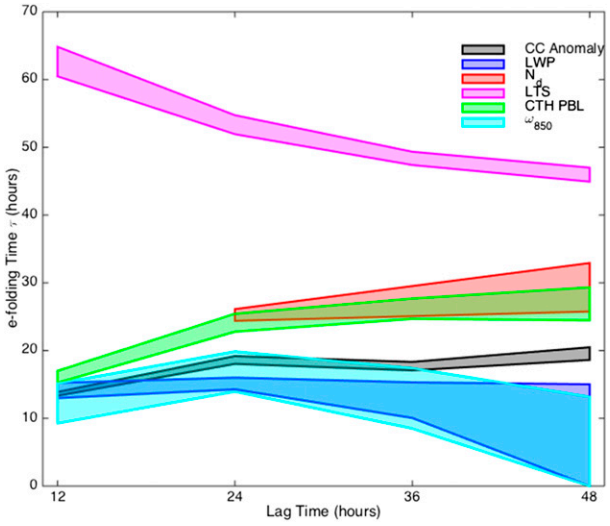

FIG. 8. Bounds for *e*-folding times τ for all variables tracked along our trajectories calculated at each lag time (sampling hours 12, 24, 36, and 48 h). Data are for trajectories that begin during the day and night for all regions combined. Error bounds are estimated using the 2-sigma confidence intervals shown in the preceding figures.

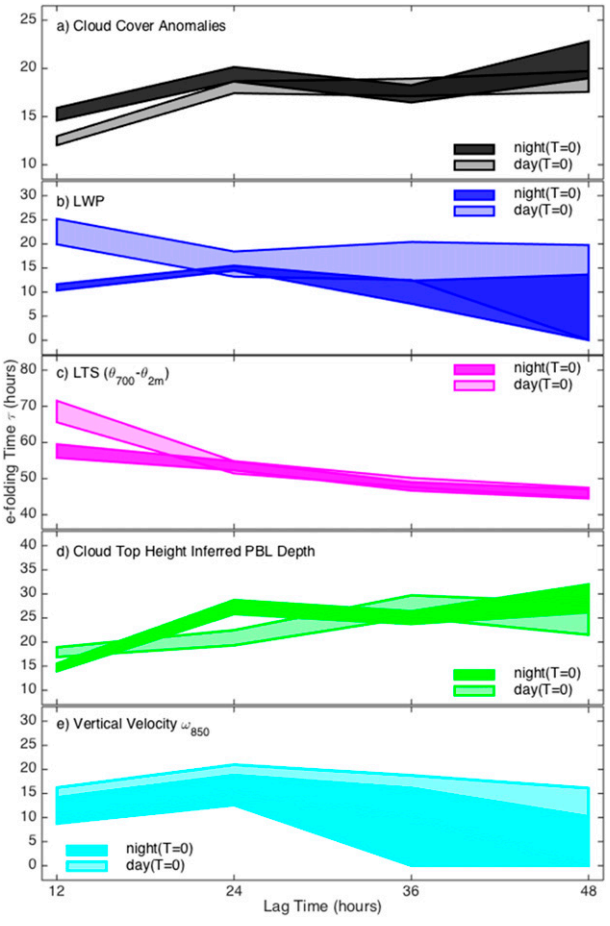

FIG. 9. Bounds for *e*-folding times τ for the five tracked variables that are sampled every 12 h. Darker plots are for trajectories that start at night (~0130 local time), and lighter plots are for trajectories that start during the day (1330 local time).

lines indicate trajectories that were observed at 0 h during the night, so at 12 h they have transitioned to day, then back to night at 24 h. There appear to be some diurnal asymmetries for each variable. Cloud cover shows slightly more persistence for 12-h transitions from night to day (during its morning breakup), while LWP, LTS, ω, and PBL depth anomalies are slightly more persistent when cloud cover is filling in during the evening. N_d is not shown since the daytime-only observations do not allow for any diurnal breakdown. LWP appears to show far more spread in τ for trajectories originating during the day, but also greater memory.

b. *Sampling radius dependence*

In all prior figures, we showed results for a 100-km sampling radius. In this section, we explore the consequences of varying that radius. In Fig. 10, we plot the mean Lagrangian decorrelation *e*-folding time for hours 24, 36, and 48 calculated for sampling radii of 100, 200, 400, 800, and 1200 km. We exclude the 12-h lag time from the mean because the 12-h τ estimates often differed significantly from the later hours. To avoid overlapping samples, we only use trajectories with starting points that are at least as far apart as the sampling diameter.

For each variable, the *e*-folding time appears to increase as the sampling radius increases. We have fit power-law approximations for the growth of τ versus sampling radius R. These power-law fits are shown as the dashed lines on the plot, with their functions shown in the legend. Memory for LWP, cloud cover, ω, N_d, and PBL depth anomalies all appear to increase similarly with sampling radius as $R^{1/3}$. For LTS anomalies, τ increases slower with increasing R, with a fit shown to be closer to $R^{1/6}$.

c. *Regional differences*

Because this study relies on data from four distinct regions, we show how *e*-folding times differ between regions in Fig. 11. Values of τ along the y axis represent the mean *e*-folding time for times 24, 36, and 48 h for each variable shown on the x axis. Cloud cover anomalies show the most consistent τ values across all four regions, while τ values for LTS appear least consistent from region to region. The *e*-folding times are shortest in the eastern Indian Ocean for every variable but ω, which shows the most consistency between regions. The southeast Pacific and southeast Atlantic appear to

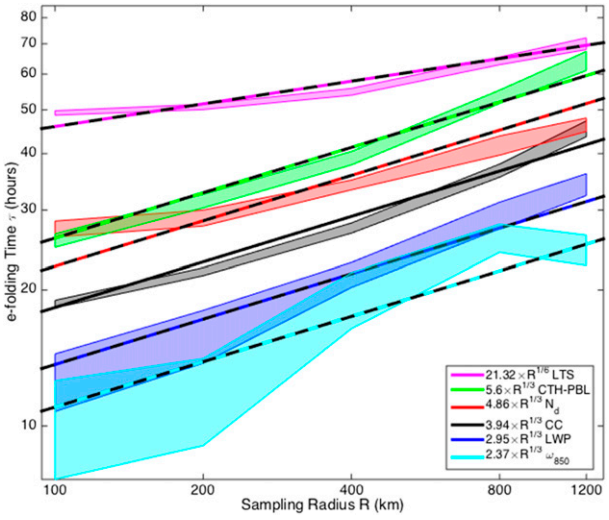

FIG. 10. Bounds for *e*-folding times τ plotted as a function of sampling radius R for all tracked variables. The *e*-folding times are the average τ for hours 24, 36, and 48. Exponential fits are plotted as the dashed lines, with their functions shown in the figure legend.

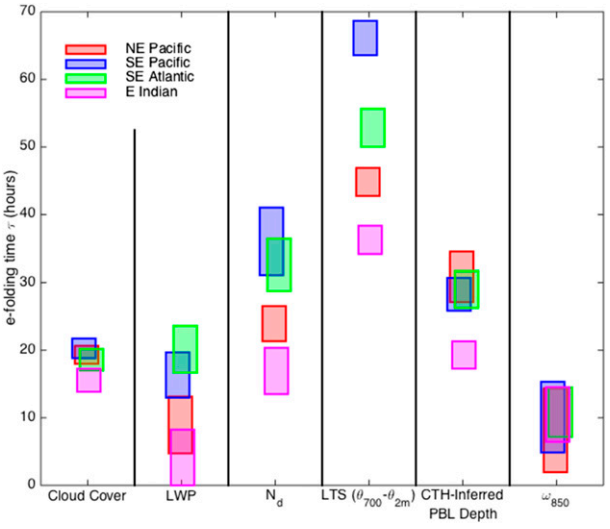

FIG. 11. Bounds for *e*-folding times τ for each tracked variable separated by region. Values of τ are the mean *e*-folding time for hours 24, 36, and 48.

behave most similarly, with overlap between τ values for five out of six variables tracked. Those two regions also show the longest *e*-folding times, except for PBL depth, where the northeast Pacific shows the strongest memory. The southeast Pacific and southeast Atlantic may show longer time scales because of their greater proximity to the equator, meaning much of the area within each box sees a weaker impact from midlatitude high-frequency "weather noise." The relative difference in τ between each variable is similar across all regions, with LWP and ω showing the shortest memory, cloud cover showing the slightly longer τ, N_d and PBL depth showing longer and nearly comparable memory, and LTS showing the longest persistence.

Section 4b shows that time scales of each variable are positively related to the spatial scales of those variables. Therefore, one possible explanation for the difference in τ values between regions is that spatial scales may vary region to region. However, a comparison of variable spatial scales (*e*-folding lengths) between regions showed no consistent, significant difference between regions.

d. Eulerian versus Lagrangian e-folding times

Figure 12 shows a comparison between the stationary, Eulerian reference frame and the Lagrangian reference frame. Stationary observations are taken at each trajectory beginning, but, rather than sampling along a trajectory, we resample the same location for 12, 24, 36, and 48 h using the same 100-km sampling radius. In Fig. 12, we plot the *e*-folding times for anomalies sampled along the trajectory alongside the *e*-folding times for the Eulerian frame of reference. The linear relationships between the mean values of initial and lagged anomalies (as in Fig. 7) are still present in the Eulerian reference frame.

Somewhat surprisingly in regards to earlier work, the *e*-folding times in the stationary (Eulerian) reference frame are either equal to or longer than the equivalent Lagrangian τ values for all variables. Eulerian τ values increase with longer lag times for cloud cover, LWP, and PBL depth, suggesting that the Eulerian anomalies are less well approximated by a red noise process. For LTS, τ declines with longer lag times for both reference frames. For N_d, the change in τ with longer lag times appears equivalent for both reference frames, though the stationary τ values are longer. Eulerian τ values are somewhat sensitive to where they are sampled along the trajectories, with larger τ values seen at the trajectory midpoints than at their beginnings (not shown).

5. Discussion

Results from this work show that cloud variables and cloud-controlling variables evolve with distinct quantifiable time scales. A red noise assumption is appropriate when variables show consistent estimated anomaly decorrelation *e*-folding times for different lag times. Figure 12 indicates that a red noise assumption for anomalies in most of our variables is a reasonable approximation in a Lagrangian reference frame, but not in a stationary reference frame, for which the persistence is longer and estimated τ increases substantially with longer lag. We can think of cloud fields evolving

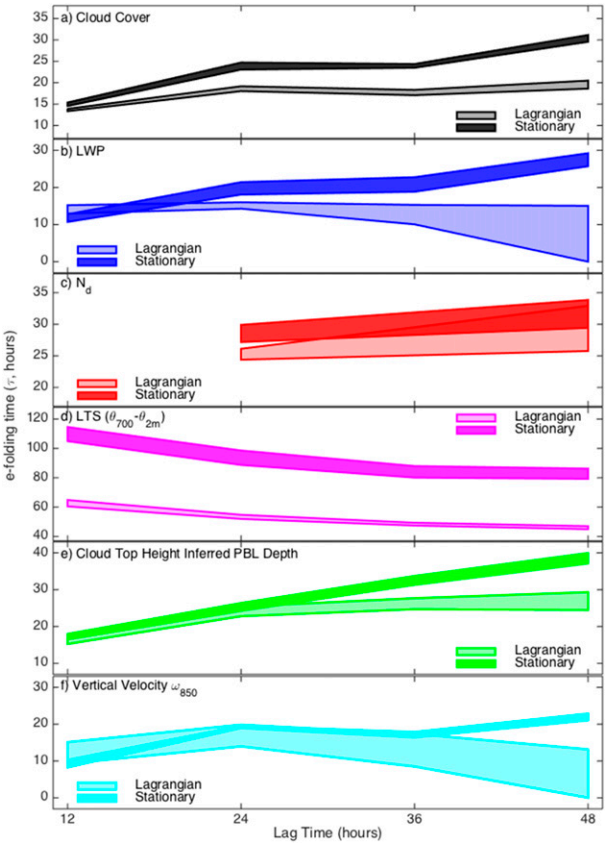

FIG. 12. Bounds for *e*-folding times τ for each tracked variable from the moving Lagrangian perspective (light) and the stationary "Eulerian" perspective (dark) plotted vs lag time.

rapidly as they advect through and respond to a relatively static spatial pattern of controlling variables.

The difference shown in *e*-folding times between the Eulerian and Lagrangian reference frames does not agree with prior studies mentioned in section 1. Mauger and Norris (2010) indicated that longer τ values would be present when following the flow, while we show that τ is actually greater at fixed locations. Methodology differences between studies may differ significantly enough to make a direct comparison impossible. Further, their study region is in the northeast Atlantic, which is a smaller Sc deck and may behave differently than the Sc regions in this study.

The Lagrangian persistence time scales of LWP and ω are similar. We suggest that this may not be coincidental, but instead reflects a response of LWP to mesoscale changes in ω, such as shallow, geostrophically balanced circulations or gravity waves. Indeed, simultaneous anomalies of LWP and $-\omega$ have a significant correlation coefficient of 0.3, suggestive of a relation we might expect: more LWP in regions of persistent anomalous ascent. Considering that ω is derived from a necessarily imperfect reanalysis, it seems likely that this correlation may be stronger. Stratocumulus thickness is also known to respond to gravity waves propagating along the inversion (e.g., Allen et al. 2013). One might anticipate a quadrature relationship with a 90° phase shift between ω and LWP (which is sensitive to inversion displacement), but the 12-h time sampling is too coarse to resolve this.

The Lagrangian persistence time scales of anomalies of N_d and PBL depth are also similar. In this case, there is less physical motivation for an underlying systematic relationship between these variables, except for their common correlation with meteorological variability. Indeed, only a weak negative correlation was seen between N_d and PBL depth. A slightly stronger correlation was found between lagged values of N_d and values of PBL depth at $T = 0$, indicating a possible eventual influence on N_d by PBL depth.

There is a curious jump in τ for PBL depth and cloud cover between 12- and 24-h lag times. This significant increase suggests the presence of other, unaccounted for cloud-controlling variables that may act to quickly degrade anomalies at shorter lag times, which this study cannot quantify because of our limited 12-hourly sampling. Further study using data with improved temporal resolution would be valuable.

We suggested a viewpoint that the Lagrangian behavior of our variables might be due to the cloud-topped boundary layer advecting through highly persistent but spatially variable anomalies of cloud-controlling factors. In this case, the Lagrangian persistence time scale of anomalies would be related to their spatial scale at a fixed time divided by a typical advection speed at which the PBL moves across these anomalies. Hence, it is valuable to compute a decorrelation length scale for each variable, which we show in Fig. 13. To produce Fig. 13, we create a vector of randomly sampled points within our regions on each day and then create a second vector for points that are a specified distance away. The points in the second vector are chosen in random directions from the initial points but are required to remain in our regions of study. We then correlate the two vectors for a variety of different separation distances to see how anomalies degrade with increasing distance. All samples are for a 100-km sampling radius. A similar approach was used by Barnes and Hartmann (2012) to characterize the scales of midlatitude eddy motions. The *e*-folding length is the distance for which the correlation coefficient between the two vectors is 1/*e*. A 1/*e* line is shown in gray on the plot.

Figure 13 shows that anomalies with short *e*-folding lengths also have short Lagrangian *e*-folding times, consistent with our viewpoint. The *e*-folding lengths for

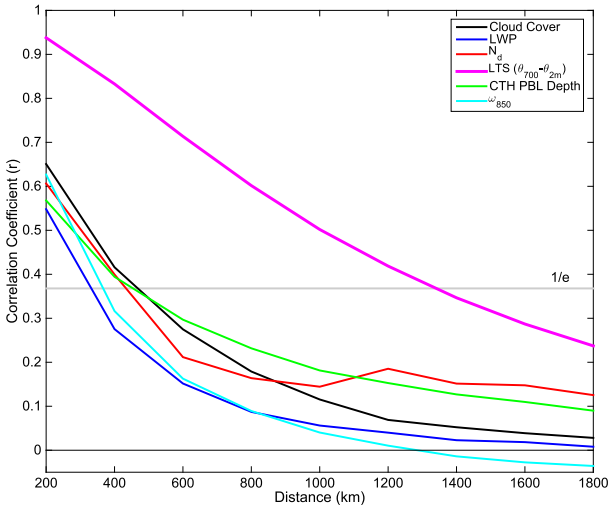

FIG. 13. Correlation coefficients r for concurrently observed vectors of tracked variables, which are set a specified distance apart during daytime in all four study regions. Data are for the years 2007–08.

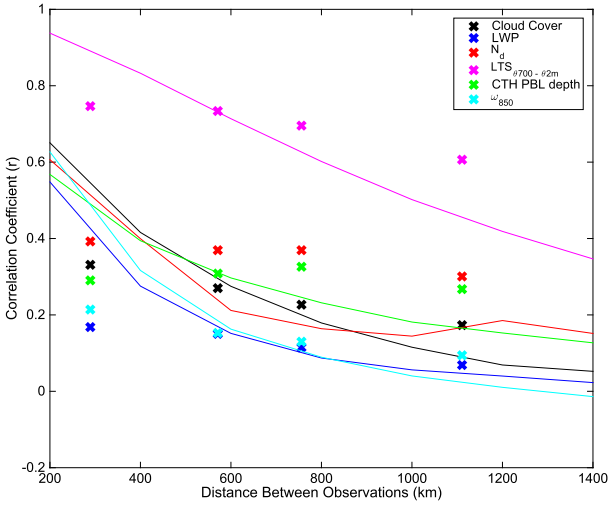

FIG. 14. Lines are as in Fig. 13. The crosses represent correlation coefficients between Lagrangian observations at $T = 0$ and $T = 24$ h for trajectories grouped by distance traveled.

LWP and ω are the smallest, at around 350 km. Cloud cover, N_d, and PBL depth anomalies show similar e-folding lengths of around 450 km, and LTS anomalies show much longer distances, nearly 1400 km. These results show that there is a relationship between the anomaly Lagrangian time scale and its decorrelation length scale.

If we assume a typical wind speed of 7 m s^{-1} in the PBL, then it would take roughly 14 h to travel 350 km (approximately the e-folding lengths for LWP and ω), which matches the Lagrangian time scales for LWP and ω. The same can be shown for cloud cover and LTS. Boundary layer depth and N_d, however, show longer "Lagrangian memories" than can be explained by the spatial scales of the fields alone, suggesting they may have internal persistence along trajectories that is not simply associated with their spatial coherence.

If spatial scales were responsible for our observed Lagrangian time scales, then we might expect that correlations between Lagrangian observations at $T = 0$ and $T = 24$ should be greater for trajectories that traveled shorter distances such that the decline in r with distance traveled along the trajectory should be similar to that shown in Fig. 13. To test this, we grouped our trajectories into four subsets based on distance traveled, then compared the correlation between Lagrangian observations at $T = 0$ and $T = 24$ h. We show these correlation coefficients as a function of mean distance traveled in Fig. 14 along with the curves from Fig. 13. Figure 14 shows that correlation coefficients do decrease as trajectory distances increase, but that the decrease with distance is not as substantial as that shown in Fig. 13, suggesting that the Lagrangian τ value is partially but not entirely predictable from the spatial scales of the cloud-controlling variables studied here.

It was hypothesized that regional differences in spatial scales could explain the differences in time scales between regions; however, a comparison of e-folding lengths between regions did not show this to be the case. No consistent regional pattern was seen for length scales.

6. Conclusions

A consistent, positive, linear relationship is seen between initial cloud anomalies and subsequently observed (lagged) anomalies when following the flow in the PBL within subtropical Sc decks. At lag times longer than 12 h, this relationship is well fit by a red noise process, in which anomalies decorrelate with a particular e-folding time scale τ. Somewhat different e-folding times are found for cloud cover ($\tau \approx 19$ h), N_d ($\tau \approx 25$–29 h), and PBL depth ($\tau \approx 24$–27 h). Lower-tropospheric stability shows a much longer memory ($\tau \approx 46$–63 h) but is less well modeled by a red noise assumption, since its apparent persistence time scale decreases with lag time. Vertical velocity and LWP show behavior similar to one another with shorter time scales ($\tau \approx 13$–17 h). LWP is also significantly correlated with $-\omega$, suggesting that ω anomalies on this time scale are a significant control on LWP.

There is some interaction of these results with the strong diurnal cycle of mean cloud and boundary layer properties, which introduces potential nonstationarity

not captured by a simple red noise process. The estimated persistence time of anomalies for cloud cover and PBL depth are shorter for a 12-h lag than for 24-h and longer lags (by 70%–80% for cloud cover and by 55%–85% for PBL depth). The *e*-folding times also depend on whether the initial sample time is at night or daytime; cloud cover shows stronger memory during morning breakup when transitioning from night to day, while all other variables show the opposite.

Different stratocumulus regions also show different behavior. Anomalies in the east Indian Ocean show shorter τ values for every variable, while the southeast Atlantic and southeast Pacific show the most similar behavior. Larger averaging regions for samples are also associated with longer Lagrangian time scales.

A comparison between the Lagrangian and Eulerian reference frame shows that anomalies appear to have more persistence at a fixed point and that a red noise assumption is accurate only when following the flow. Spatial decorrelation scales of cloud-related variables are strongly related to their Lagrangian temporal decorrelation scales. A conceptual model in which the Lagrangian time scale is predicted by the spatial decorrelation scale and the advection speed is qualitatively, but not quantitatively, accurate in understanding these relationships.

Acknowledgments. This work was supported by NASA Grant NNXBAQ35G and NSF Grant AGS-1445813. Rhea George provided trajectory code.

REFERENCES

Allen, G., and Coauthors, 2013: Gravity-wave-induced perturbations in marine stratocumulus. *Quart. J. Roy. Meteor. Soc.*, **139**, 32–45, doi:10.1002/qj.1952.

Barnes, E. A., and D. L. Hartmann, 2012: The global distribution of atmospheric eddy length scales. *J. Climate*, **25**, 3409–3416, doi:10.1175/JCLI-D-11-00331.1.

Berner, A. H., C. S. Bretherton, R. Wood, and A. Muhlbauer, 2013: Marine boundary layer cloud regimes and POC formation in a CRM coupled to a bulk aerosol scheme. *Atmos. Chem. Phys.*, **13**, 12 549–12 572, doi:10.5194/acp-13-12549-2013.

Bretherton, C. S., and M. C. Wyant, 1997: Moisture transport, lower-tropospheric stability, and decoupling of cloud-topped boundary layers. *J. Atmos. Sci.*, **54**, 148–167, doi:10.1175/1520-0469(1997)054<0148:MTLTSA>2.0.CO;2.

——, R. Wood, R. C. George, D. Leon, G. Allen, and X. Zheng, 2010: Southeast Pacific stratocumulus clouds, precipitation and boundary layer structure sampled along 20°S during VOCALS-REx. *Atmos. Chem. Phys.*, **10**, 10 639–10 654, doi:10.5194/acp-10-10639-2010.

Chan, K. M., and R. Wood, 2013: The seasonal cycle of planetary boundary layer depth determined using COSMIC radio occultation data. *J. Geophys. Res. Atmos.*, **118**, 12 422–12 434, doi:10.1002/2013JD020147.

Dee, D. P., and Coauthors, 2011: The ERA-Interim reanalysis: Configuration and performance of the data assimilation system. *Quart. J. Roy. Meteor. Soc.*, **137**, 553–597, doi:10.1002/qj.828.

Eastman, R., and R. Wood, 2016: Factors controlling low cloud evolution over the eastern subtropical oceans: A Lagrangian perspective using the A-Train satellites. *J. Atmos. Sci.*, **73**, 331–351, doi:10.1175/JAS-D-15-0193.1.

Hanna, S. R., 1981: Lagrangian and Eulerian time-scale relations in the daytime boundary layer. *J. Appl. Meteor.*, **20**, 242–249, doi:10.1175/1520-0450(1981)020<0242:LAETSR>2.0.CO;2.

Hasselmann, K., 1976: Stochastic climate models. Part I. Theory. *Tellus*, **28A**, 473–485, doi:10.1111/j.2153-3490.1976.tb00696.x.

Hubanks, P. A., M. D. King, S. Platnick, and R. Pincus, 2008: MODIS Atmosphere L3 gridded product algorithm theoretical basis document. MODIS Tech. Doc. ATBD-MOD-30, 96 pp. [Available online at http://modis-atmos.gsfc.nasa.gov/_docs/L3_ATBD_2008_12_04.pdf.]

Jenkins, G. M., and D. G. Watts, 1968: *Spectral Analysis and Its Applications*. Holden-Day, 523 pp.

Karlsson, J., G. Svensson, S. Cardoso, J. Teixeira, and S. Paradise, 2010: Subptropical cloud-regime transitions: Boundary layer depth from cloud-top height evolution in models and observations. *J. Appl. Meteor. Climatol.*, **49**, 1845–1858, doi:10.1175/2010JAMC2338.1.

King, M. D., and Coauthors, 2003: Cloud and aerosol properties, precipitable water, and profiles of temperature and humidity from MODIS. *IEEE Trans. Geosci. Remote Sens.*, **41**, 442–458, doi:10.1109/TGRS.2002.808226.

Mann, M. E., and J. M. Lees, 1996: Robust estimation of background noise and signal detection in climatic time series. *Climatic Change*, **33**, 409–445, doi:10.1007/BF00142586.

Mauger, G. S., and J. R. Norris, 2010: Assessing the impact of meteorological history on subtropical cloud fraction. *J. Climate*, **23**, 2926–2940, doi:10.1175/2010JCLI3272.1.

Myers, T. A., and J. R. Norris, 2013: Observational evidence that enhanced subsidence reduces subtropical marine boundary layer cloudiness. *J. Climate*, **26**, 7507–7524, doi:10.1175/JCLI-D-12-00736.1.

Oreopoulos, L., 2005: The impact of subsampling on MODIS level-3 statistics of cloud optical thickness and effective radius. *IEEE Trans. Geosci. Remote Sens.*, **43**, 366–373, doi:10.1109/TGRS.2004.841247.

Partain, P., 2007: *CloudSat* MODIS-AUX auxiliary data process description and interface control document. Cooperative Institute for Research in the Atmosphere, Colorado State University, 23 pp.

Platnick, S., M. D. King, S. A. Ackerman, W. P. Menzel, B. A. Baum, J. C. Riédi, and R. A. Frey, 2003: The MODIS cloud products: Algorithms and examples from *Terra*. *IEEE Trans. Geosci. Remote Sens.*, **41**, 459–473, doi:10.1109/TGRS.2002.808301.

Roe, G., 2009: Feedbacks, timescales, and seeing red. *Annu. Rev. Earth Planet. Sci.*, **37**, 93–115, doi:10.1146/annurev.earth.061008.134734.

Sun-Mack, S., P. Minnis, Y. Chen, S. Kato, Y. Yi, S. C. Gibson, P. W. Heck, and D. M. Winker, 2014: Regional apparent boundary layer lapse rates determined from *CALIPSO* and MODIS data for cloud-height determination. *J. Appl. Meteor. Climatol.*, **53**, 990–1011, doi:10.1175/JAMC-D-13-081.1.

Vaughan, M., S. Young, D. Winker, K. Powell, A. Omar, Z. Liu, Y. Hu, and C. Hostetler, 2004: Fully automated analysis of space-based lidar data: An overview of the *CALIPSO* retrieval algorithms and data products. *Laser Radar Techniques for Atmospheric Sensing*, U. N. Singh, Ed., International Society

for Optical Engineering (SPIE Proceedings, Vol. 5575), 16–30, doi:10.1117/12.572024.

von Storch, H., and F. W. Zwiers, 1999: *Statistical Analysis in Climate Research*. Cambridge University Press, 484 pp.

Wentz, F. J., and T. Meissner, 2004: AMSR-E/*Aqua* L2B Global Swath Ocean Products derived from Wentz Algorithm, version 2. NASA National Snow and Ice Data Center Distributed Active Archive Center, accessed September 2015, doi:10.5067/AMSR-E/AE_OCEAN.002.

Wood, R., and C. S. Bretherton, 2004: Boundary layer depth, entrainment, and decoupling in the cloud-capped subtropical and tropical marine boundary layer. *J. Climate*, **17**, 3576–3588, doi:10.1175/1520-0442(2004)017<3576:BLDEAD>2.0.CO;2.

Wunsch, C., 1999: The interpretation of short climate records, with comments on the North Atlantic and Southern Oscillations. *Bull. Amer. Meteor. Soc.*, **80**, 245–255, doi:10.1175/1520-0477(1999)080<0245:TIOSCR>2.0.CO;2.

Wyant, M. C., C. S. Bretherton, H. A. Rand, and D. E. Stevens, 1997: Numerical simulations and a conceptual model of the stratocumulus to trade cumulus transition. *J. Atmos. Sci.*, **54**, 168–192, doi:10.1175/1520-0469(1997)054<0168:NSAACM>2.0.CO;2.